Structural phase transitions and dielectric properties of $BaTiO_3$ from a second-principles method

Jingtong Zhang,[1,2,3] Louis Bastogne,[2] Xu He,[2] Gang Tang,[2,4] Yajun Zhang,[5,6] Philippe Ghosez,[2,*] and Jie Wang[1,3,7,†]

[1]*Zhejiang Laboratory, Hangzhou 311100, Zhejiang, China*

[2]*Theoretical Materials Physics, Q-MAT, CESAM, Université de Liège, B-4000 Liège, Belgium*

[3]*Department of Engineering Mechanics, School of Aeronautics and Astronautics, Zhejiang University, Hangzhou 310027, Zhejiang, China*

[4]*Advanced Research Institute of Multidisciplinary Science, Beijing Institute of Technology, Beijing 100081, China*

[5]*Department of Mechanics and Engineering Science, College of Civil Engineering and Mechanics, Lanzhou University, Lanzhou 730000, Gansu, China*

[6]*Key Laboratory of Mechanics on Disaster and Environment in Western China Attached to The Ministry of Education of China, Lanzhou University, Lanzhou 730000, Gansu, China*

[7]*Key Laboratory of Soft Machines and Smart Devices of Zhejiang Province, Zheda Road 38, Hangzhou, Zhejiang 310027, China*

(Received 1 August 2023; accepted 28 September 2023; published 26 October 2023)

Barium titanate ($BaTiO_3$, BTO) is a typical ferroelectric material with a series of complex phase transitions. Understanding its phase transitions and related properties from an atomic perspective is of scientific significance and practical importance. In this paper, based on first-principles calculation, a second-principles model is constructed to investigate the phase transition and related properties of BTO at the atomic level. By using the constructed second-principles model, the full phase-transition sequence from high-temperature paraelectric cubic phase to the low-temperature rhombohedral phase through tetragonal and orthorhombic intermediate phases have been successfully predicted at the atomic level. To reveal the underlying mechanism of phase transition, the influences of different anharmonic terms on phase transition are investigated in detail. We found that the interaction between strain and Ti-O bond plays an essential role in phase transition. Furthermore, dielectric properties and the *P-E* loop of BTO are successfully obtained with the model. In this paper, we not only provide a model to predict the phase transitions and related properties of BTO from the atomic level but also extend the application of the second-principles method.

DOI: 10.1103/PhysRevB.108.134117

I. INTRODUCTION

Perovskite oxides are a class of materials following the ABO_3 formula, which have received much attention due to their multifunctional properties, such as ferroelectric, piezoelectric, dielectric, and magnetoelectric properties [1–4]. Barium titanate ($BaTiO_3$, BTO) is one of the most representative perovskite oxides and has been widely investigated due to its rich and complex ferroelectric phase transition [5]. At a temperature >398 K, BTO is paraelectric and has a cubic structure with the *Pm*3*m* space group. When the temperature gradually decreases, BTO undergoes three phase transitions, namely, from cubic phase to the tetragonal *P*4*mm* phase at 398 K, from the tetragonal phase to the orthorhombic *Amm*2 phase at 281 K, and from the orthorhombic phase to the rhombohedral *R*3*m* phase at 202 K [6]. Compared with the temperature-driven phase transitions of other perovskite materials such as $PbTiO_3$ or $SrTiO_3$, the phase transition of BTO is much more complicated and is challenging to accurately model.

To investigate the phase transition and related properties of ferroelectric materials at atomistic level, first-principles calculations based on density functional theory (DFT) are widely used in the literature. The double well energy surface was calculated by first-principles calculation for BTO [7]. After that, first-principles calculations had been devoted to predicting the structure, energy, polarization of different phases of BTO [8,9], but these calculations were restricted to zero temperature. Although finite-temperature properties can be studied via *ab initio* molecular dynamics (MD) [9,10], the expensive computational cost limits the simulation system to hundreds of atoms and prevents the study of the phase transition of BTO at larger time and length scales.

To overcome these limitations and investigate the complex series of phase transitions of BTO, several approaches have been proposed, such as the thermodynamic Landau-Ginsburg-Devonshire (LGD) model [11,12], the effective Hamiltonian method [13,14], the core-shell model [15,16], and the bond-valence model [17]. The LGD approach can predict the same phase-transition sequence as experimental observation [12]. Nevertheless, the empirical parameters of the LGD model need to be determined from experiments. Furthermore, as a phenomenological model, it also cannot reveal the mechanisms of material behavior at the atomic level. To avoid empirical parameters, a first-principles-based effective Hamiltonian method was developed to study the temperature phase diagram of BTO by Zhong *et al.* [14]. Although the effective Hamiltonian method successfully captured the

*Philippe.Ghosez@uliege.be

†jw@zju.edu.cn

phase-transition sequence of BTO, the phase-transition temperature T_c is underestimated. Moreover, this method is limited to a restricted subspace, implying the contribution from other lattice distortions is ignored. As a result, it failed to describe the heat expansion [18].

The core-shell model [19] and bond-valence theory [20] were also used to investigate the phase transition of BTO. Although both have captured the phase-transition sequence of BTO, the phase-transition temperatures tend to be too small when comparing with experiment data [16,17]. Recently developed machine-learning-based methods [21–24] have also been applied to study the phase transition and dielectric response of BTO [22]. However, due to the uninterpretability of machine learning models, this method for BTO can only characterize the properties of a material without a clear physical interpretation. Moreover, this method is computationally intensive and was only applied on a small supercell ($6 \times 6 \times 6$). Since the phase-transition temperature changes with cell size when it is not large enough, a small supercell is not conductive to study phase transitions [13].

The limitation of the above methods can be overcome to some extent by the second-principles method. The second-principles method is an atomic model based on a Taylor expansion of the potential energy surface around a reference structure [25]. This method includes many more degrees of freedom than the effective Hamiltonian method, which can describe more properties of materials, especially those related to high-frequency modes. Moreover, the second-principles method makes full use of phonon dispersion of a reference structure from density functional perturbation theory (DFPT) calculations, which means that all the coefficients of the harmonic part are exact. The computational cost of this method is less, and we can study larger systems than a machine learning model or *ab initio* MD. The second-principles models have been built for $CaTiO_3$, $PbTiO_3$, $SrTiO_3$, and PTO/STO superlattices, which have been used to study the negative capacitance [26], polar skyrmions [27], and energy storage [28] of the materials. However, as one of the most typical ferroelectric materials with complex phase-transition characters, the second-principles model for BTO is absent.

In this paper, a second-principles model for BTO is constructed based on the potential energy surface from first-principles calculation. The accuracy of this model is examined by comparing with first-principles calculations. The finite-temperature properties of BTO, such as structural phase transition, and dielectric properties are studied by the model. The model successfully captures the series of phase transitions. The phase-transition temperature is very consistent with experimental results after hydrostatic pressure is added to the model. The relationship between different anharmonic energy terms and temperature are studied, which provides deep insight into the phase transitions of BTO.

II. METHODOLOGY

A. First-principles calculations

First-principles calculations are performed using the ABINIT package [29,30] with a cutoff energy of 40 Ha. PBEsol is used as the electron exchange-correlation potential [31]. Valence electrons of Ba ($5s^2\,5p^6\,6s^2$), Ti($3s^2\,3p^6\,3d^2\,4s^2$), and O($2s^2\,2p^4$) are used in the calculation. The Brillouin zone is sampled with an $8 \times 8 \times 8$ k-point grid for a unit cell and a $4 \times 4 \times 4$ k-point grid for a $2 \times 2 \times 2$ supercell. In the relaxation, the structures are fully optimized until all the forces on the atoms are $<10^{-6}$ Ha/Bohr. The interatomic force constants and Born effective charges are obtained by DFPT in the ABINIT package [32]. The phonon dispersions are computed using the ANADDB program [33,34].

B. Second-principles calculations

The first step of the second-principles method is to generate a model that describes the potential energy surface around the reference structure as a function of all the displacements of atoms and strain [25]. The harmonic terms of this model are obtained directly from phonon dispersion calculated by first-principles calculations. The anharmonic terms are fitted on a series of DFT calculated configurations, which can be called training set. The second step is to carry out molecular dynamic simulations to predict behavior of materials at finite temperature. Due to the periodic boundary conditions used during the fitting procedure and MD simulations, this model is used for bulk materials. In this paper, our model is generated by the software package MULTIBINIT, which is released within the ABINIT package [30]. The ideal cubic phase is selected as the reference structure. The harmonic energy terms are obtained from phonons of reference structure. The phonon dispersion from DFT calculation of the cubic phase is shown in Fig. 1(a). All the unstable modes in phonon dispersion indicate that the second derivatives of energy are negative. Therefore, the M, X, and Γ points of the cubic Brillouin zone need to be considered when building the training set. The training set we used contains 741 different lattice configurations. As is shown in Fig. 1(b), the training set includes 15 nodes and configurations generated from the linear interpolation between them. These nodes include cubic, tetragonal, orthorhombic, and rhombohedral phases of BTO; three directions of M and X points of the Brillouin zone; two 90 ° domains; and three configurations in which only one atom is moved.

To get better performance from the second-principles model, the maximum energy of configurations is selected to be $<$81.6 meV per unit cell above the reference structure, which is about three times of the energy of the rhombohedral phase, and the configurations with higher energy are excluded from the training set. The total energies of the training set are shown by the blue dots in Fig. 2(a). During the fitting procedure, the cutoff is selected to be 2.89 Å, which is $\frac{\sqrt{2}}{2}a_0$, and 18 anharmonic terms are chosen. The final convergence value of the goal function with respect to forces and stresses is $2.38 \times 10^{-4}\,\mathrm{eV}^2/\mathrm{Å}^2$, which seems to be good enough compared with the second-principles model for $SrTiO_3$ [35]. The mean standard deviation value of the effective potential with respect to the training set is $4.7177\,\mathrm{meV}^2$ per atom after the fitting procedure. All the generated anharmonic terms and their parameters are listed in Table I.

Figures 2(a) and 2(b) give the comparison of energies between DFT calculations and the second-principles model. The average energy difference is 1.19 meV/f.u., and most of the differences originate from the underestimation at the lower-energy region. After that, the bounding procedure is

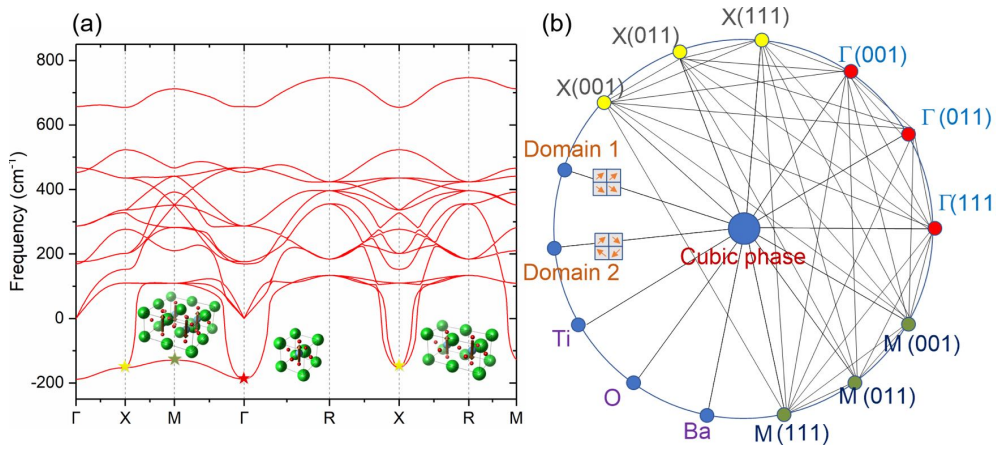

FIG. 1. (a) Phonon dispersion of cubic $BaTiO_3$ obtained from first-principles calculations. The arrows in the insets show the corresponding displacements of Ti atoms. (b) Sketch of the training set. Each node represents a structure, and the solid line between nodes represents the linear interpolation between two structures.

applied to avoid potential divergence problems. The bounding procedure checks all the anharmonic terms, and if the parameter of the highest-order terms is negative, this procedure will add new higher-order terms to the model and prevent the energy of the model from going to negative infinity. After the bounding procedure, 64 high-order anharmonic terms are added to the model, and they are listed in Table S1 in the Supplemental Material [36]. Figure 2(c) gives the energies of

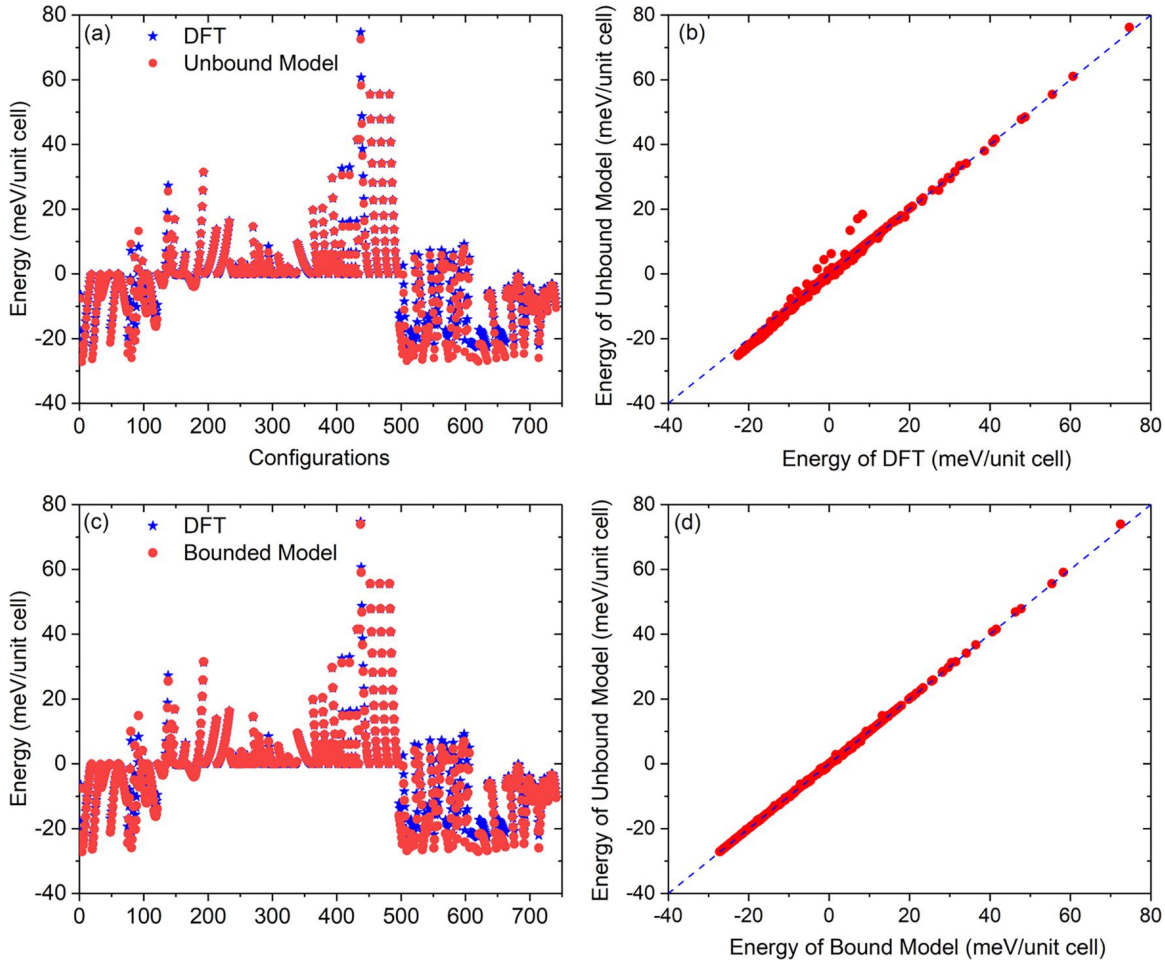

FIG. 2. Total energies of the training set from density functional theory (DFT) calculations and their comparison with (a) and (b) unbound second-principles model and (c) bounded second-principles model. (d) Energy comparison between bounded and unbounded second-principles model.

TABLE I. Anharmonic terms and their parameters.

No.	Parameters	Anharmonic terms
1	$-5.7929374644\times10^{-2}$	$(\mathrm{Ba}_x-\mathrm{O}_{1x})^2\eta_1$
2	$-5.3329546486\times10^{-3}$	$(\mathrm{Ba}_x-\mathrm{O}_{1x})^2(\mathrm{Ba}_x-\mathrm{O}_{1x}[0,\ 0,\ -1])^2$
3	$3.4168544341\times10^{-2}$	$(\mathrm{Ba}_x-\mathrm{O}_{1x})(\mathrm{Ba}_x-\mathrm{O}_{1x}[0,\ 0,\ -1])\eta_1$
4	$2.9066257673\times10^{-3}$	$(\mathrm{Ba}_x-\mathrm{O}_{1x})^3(\mathrm{Ba}_x-\mathrm{O}_{1x}[0,\ 0,\ -1])$
5	$-2.6344794045\times10^{-2}$	$(\mathrm{Ba}_x-\mathrm{O}_{1x})^2\eta_2$
6	$8.9170528880\times10^{-4}$	$(\mathrm{Ba}_x-\mathrm{O}_{1x})^4$
7	$1.5531687831\times10^{-2}$	$(\mathrm{Ti}_x-\mathrm{O}_{1x})^3(\mathrm{Ti}_x-\mathrm{O}_{2x})$
8	$-5.9597829673\times10^{-1}$	$(\mathrm{Ti}_x-\mathrm{O}_{1x})(\mathrm{Ti}_x-\mathrm{O}_{1x}[1,\ 0,\ 0])\eta_1$
9	$1.3005784211\times10^{-2}$	$(\mathrm{Ti}_x-\mathrm{O}_{1x})^2(\mathrm{Ti}_y-\mathrm{O}_{2y})^2$
10	$-3.7937624116\times10^{-2}$	$(\mathrm{Ti}_y-\mathrm{O}_{1y})(\mathrm{Ti}_x-\mathrm{O}_{2x})\eta_6$
11	$-8.1917338897\times10^{-2}$	$(\mathrm{Ti}_x-\mathrm{O}_{1x})^2\eta_2$
12	$4.5137690189\times10^{-2}$	$(\mathrm{Ti}_x-\mathrm{O}_{1x})(\mathrm{Ti}_x-\mathrm{O}_{2x})\eta_2$
13	$1.2423922774\times10^{-2}$	$(\mathrm{Ti}_x-\mathrm{O}_{1x})^2(\mathrm{O}_{1x}-\mathrm{O}_{2x}[-1,\ 1,\ 0])^2$
14	$-3.4742146459\times10^{-2}$	$(\mathrm{Ti}_x-\mathrm{O}_{1x})^3$
15	$-2.5410991693\times10^{-2}$	$(\mathrm{Ti}_y-\mathrm{O}_{1y})^2\eta_3$
16	$6.9615236200\times10^{-3}$	$(\mathrm{Ba}_x-\mathrm{O}_{1x})(\mathrm{Ti}_x-\mathrm{O}_{1x})\eta_2$
17	$-1.3126444251\times10^{-3}$	$(\mathrm{Ba}_x-\mathrm{O}_{1x})(\mathrm{Ti}_x-\mathrm{O}_{1x})^3$
18	$-1.4073204203\times10^{-2}$	$(\mathrm{O}_{1x}-\mathrm{O}_{2x})^2\eta_1$

the training set from the bounded model and their comparison with DFT calculations. The bounding procedure slightly raises the average energy difference to 1.20 meV/f.u., and the comparison with the results of the unbounded model is shown in Fig. 2(d). All the points are on a straight line at $x = y$, indicating that the bounding procedure has almost no influence on the potential energy surface.

C. MD simulations

The MD simulations are carried out on $16\times16\times16$ supercell that contains 20 480 atoms with periodic boundary conditions. The isobaric-isothermal (NPT) ensemble is adopted. For structural phase transitions, the simulations begin at 10 K and proceed in steps of 10 K increments until the temperature arrives at 450 K. Here, 20 000 MD steps, which is equal to 24.2 ps, are used for each temperature. We checked that 20 000 MD steps are large enough to converge the energy and pressure, as is shown in Figs. S1 and S2 in the Supplemental Material [36]. The average of the last 10 000 MD steps is used to obtain the lattice constant, polarization, and the initial structure of the next temperature step. For dielectric properties, the simulations are carried out on the tetragonal phase of BTO. The simulation begins at 210 K and proceeds in steps of 1 K increments until the temperature reaches 250 K. The electric fields are applied on z-direction ranges from 0.004 to -0.004 V/Å for dielectric properties and 0.0085 to -0.0085 V/Å for P-E loops.

III. RESULTS AND DISCUSSION

A. Model validation

First, the second-principles model is validated by comparing the calculated ground-state structure with the DFT and experiment results. As is shown in Table II, although the energy obtained from our model is slightly lower than the DFT result, the lattice constant and unit cell volume agree well

TABLE II. Ground state properties from DFT, second-principles model, and experiment.

	DFT	Second principles	Experiment [37]
Lattice constant (Å)	3.993	3.9945	4.004
Angle	89.858	89.842	89.839
Volume (Å^3)	63.675	63.739	64.234
E_{tot} (meV)	−23.102	−27.955	–
Polarization (μC/cm^2)	42.93	44.89	–

with the DFT and experimental results, which are measured at 15 K [37]. Next, all the identified metastable phases of BTO from DFT calculations are relaxed with the second-principles model. All the local minima energies with respect to the cubic phase are compared, as is shown in Fig. 3. The phases with symmetries $P4mm$, $Amm2$, and $R3m$ correspond to three polar phases in BTO, which represent the tetragonal, orthorhombic, and rhombohedral phases, respectively. The phases with symmetries $P4/nmm$ and $Pmma$ correspond to antipolar motions of Ti atoms along z directions. The phases with symmetries $Cmcm$ and $Pbcm$ correspond to antipolar motions of Ba and Ti atoms along y and z directions. Although the energies obtained from the second-principles model are lower than DFT calculations, the order of energy from highest to lowest is the same, which is essential for reproducing the phase-transition sequence. The ISOTROPY program is used for the space group analysis [38]. The amplitudes of different modes are shown in Fig. 4. These results indicate that our model reproduces the same structure as DFT results at local minima.

Furthermore, we compare the phonon dispersions of tetragonal, orthorhombic, rhombohedral, and cubic phases obtained from the bounded second-principles model with those of *ab initio* DFPT calculations. The phonon dispersions from the second-principles model are calculated with the PHONOPY

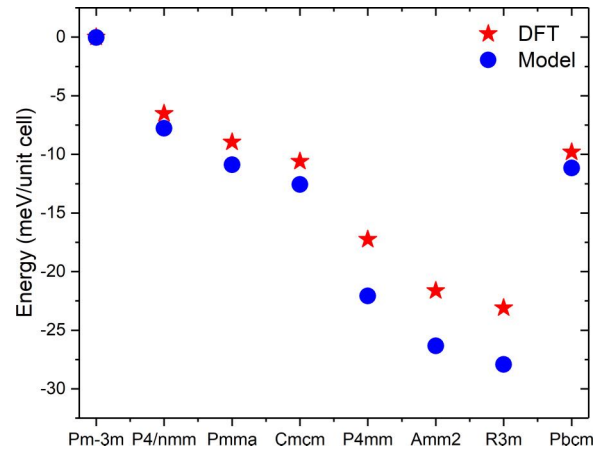

FIG. 3. Comparison of total energies for different phases from density functional theory (DFT) calculation and bounded second-principles model. It should be noticed that the structures at which the energies are calculated from DFT and second-principles model are fully relaxed to obtain the local minimum.

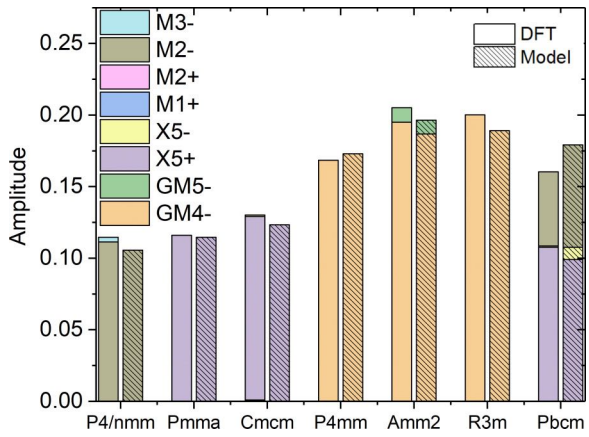

FIG. 4. Amplitude of different modes for the local minimum from density functional theory (DFT) calculation and second-principles model. The color represents the proportion of different modes, and the rectangle with/without slash are the results from model/DFT.

program [39,40]. As is shown in Fig. 5, the phonon dispersion of our model coincides quite well with the DFT calculation, and the band gap and widths are well reproduced by our model; these results ensure the validity of our models. It should be noticed that there is almost no difference between DFT and the second-principles model on the phonons of the cubic phase since the harmonic terms are directly obtained from DFT calculations and the reference structure is the cubic phase. Moreover, from Fig. 5(c), it can be seen clearly that there is no extra unstable mode in the phonon dispersion of the rhombohedral phase, which indicates that our model is sufficient to provide a precise potential energy surface around the ground state. We also checked the phonon dispersion from the unbounded second-principles model, as is shown in Fig. S3 in the Supplemental Material [36]; both bounded and unbounded models provide similar phonon dispersions for the ground state, which indicates the bounding procedure only has little influence on potential energy surface.

B. Structural phase transition

After the validation of the model, the temperature-dependent phase transitions of BTO were investigated. The polarization and lattice constant changes with temperature from the bounded model are shown in Fig. 6. The results from the unbounded model are shown in Figs. S4 and S5 in the Supplemental Material [36]. At low temperature, the polarization is aligned along the [111] direction, which indicates a rhombohedral phase. When the model is heated up to 140 K, a sudden decrease of P_y, which is accompanied by the changes in lattice constants, indicates a phase transition to the orthorhombic phase. After that, two additional phase transitions occur at 180 and 224 K, which are the phase

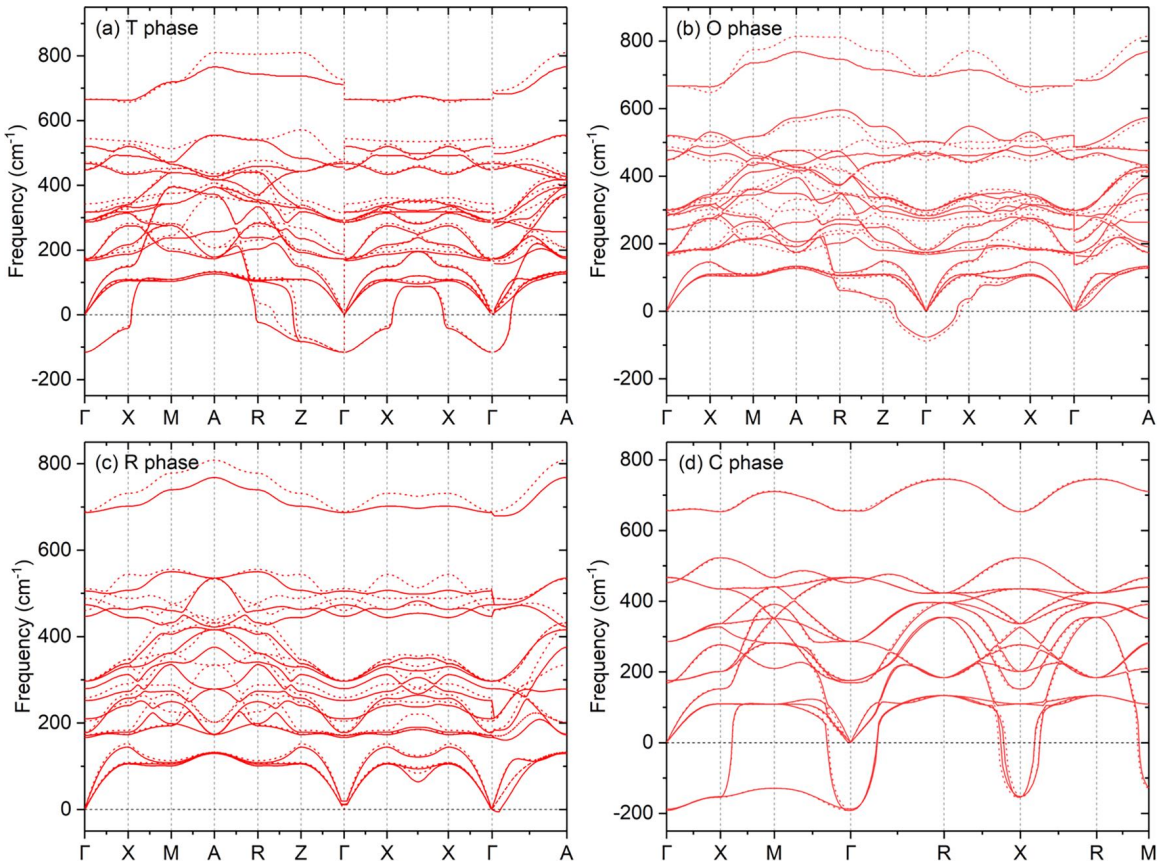

FIG. 5. Comparison of phonon dispersion at (a) tetragonal, (b) orthorhombic, (c) rhombohedral, and (d) cubic phase. The dash line is calculated by second-principles model while the solid line is obtained from DFT calculations.

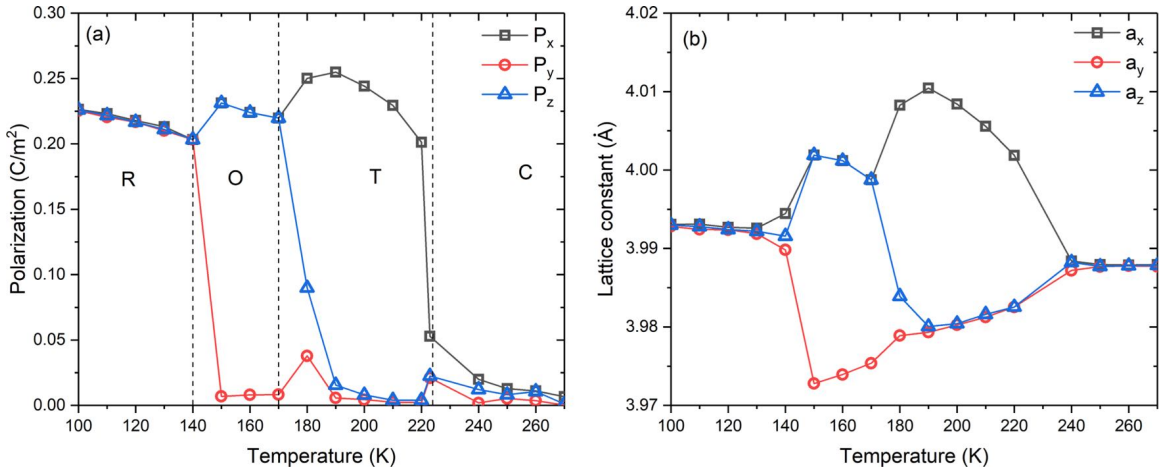

FIG. 6. (a) Polarization and (b) lattice constant changes with temperature from bounded second-principles model.

transitions from orthorhombic to tetragonal and tetragonal to cubic, respectively. The sequence of phase transitions from the second-principles model is the same as that observed from experiment. Moreover, the lattice constants increase slowly when the temperature is >224 K, which indicates that our second-principles model can describe thermal expansion, while the effective Hamiltonian method failed to do so [25].

Next, we compare our simulations with the results from the literature, which also used PBEsol as the exchange-correlation functional. The phase-transition temperatures from different methods are listed in Table III. It can be seen clearly that all the methods underestimate the phase-transition temperature except a recently developed effective Hamiltonian model with anharmonic terms. This anharmonic effective Hamiltonian model introduces anharmonic terms up to the eighth order, and after the comparison, we found that, although there are also eighth-order terms in our model after the bounding procedure, they have almost no influence on the potential energy surface, which can be seen clearly from Fig. 2(d), since they are introduced to the model through the bounding procedure instead of the fitting procedure. Thus, the underestimate in the phase-transition temperature might result in the truncation at the fourth order during the fitting procedure.

The negative hydrostatic pressure has been used to compensate underestimation of the local density approximation result for the cubic lattice constant in the effective Hamiltonian method or the second-principles model of $PbTiO_3$ [14,25]. Since the lattice constant for the cubic phase from PBEsol is also slightly lower than that from experiment, we carried out MD simulations under negative hydrostatic pressure. The polarization and lattice constant changes with temperature under −5 Gpa are shown in Fig. 7. The sequence of phase transitions is still observed to be R-O-T-C, and the phase-transition temperature is much closer to experimental results. The pressure-temperature phase diagram is shown in Fig. 8. The phase-transition temperature changes linearly with applied hydrostatic pressure, and the critical pressure when the phase transitions disappears is 7 Gpa. Comparisons between experiment and the effective Hamiltonian method on dT_c/dP for different phase transitions are listed in Table IV [14,43]. Although our model gets almost the same value on dT_c/dP of the O-T phase transition, it fails to correctly reproduce two other phase transitions on dT_c/dP. Since our model is based on the Taylor expansion of the potential energy surface, the omission of high-order terms might be the reason for this difference. Moreover, in Ref. [14], the difference on dT_c/dP between experimental and simulation is attributed to the neglect of higher-order strain coupling terms. Although high-order terms are applied to our model by the bounding procedure, as shown in Table S1 in the Supplemental Material [36], they have little influence on the model. The high-order strain coupling terms are still neglected in our model, as shown in Table I. Therefore, improving the accuracy of the phase diagram might require adding high-order strain coupling terms during the fitting procedure, which will be studied in the future.

TABLE III. Comparison of phase-transition temperatures from different methods that used PBEsol as the exchange-correlation functional and experiment.

	R-O	O-T	T-C
Second-principles method (this paper)	140 K	180 K	224 K
Machine learning model [22]	18.6 K	91.4 K	182.4 K
Effective Hamiltonian [41]	119 K	158 K	257 K
Core-shell model [16]	150 K	210 K	260 K
Bond-valence model [17]	100 K	110 K	160 K
Effective Hamiltonian (anharmonic) [41]	186 K	255 K	395 K
Experiment [42]	183 K	278 K	403 K

TABLE IV. dT_c/dP from this paper and the literature.

	This Paper	Effective Hamiltonian Method from Ref. [14]	Experiment from Ref. [43]
R-O (K/Gpa)	−27	−15	−15
O-T (K/Gpa)	−29	−22	−28
T-C (K/Gpa)	−30	−28	−40

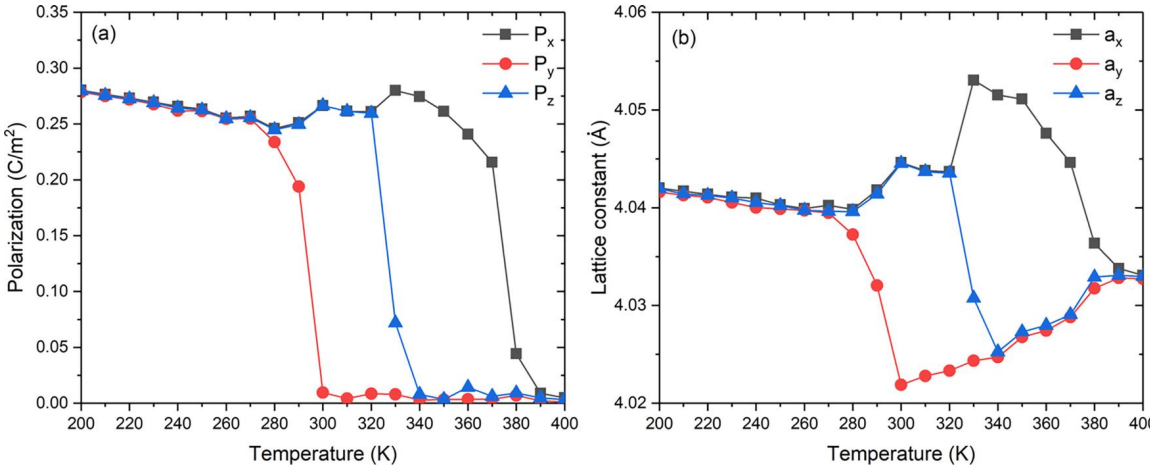

FIG. 7. Polarization changes with temperature from bounded second principles model under −5 Gpa pressure.

C. Roles of different interactions

The balance between long- and short-range interactions is believed to be the origin of ferroelectricity [44]. Weakening or strengthening them can greatly change phase-transition properties of ferroelectric materials. Based on the effective Hamiltonian method, it has been found that elimination of the long-range interaction can lead to an antiferroelectric phase, and the accuracy of the short-range interaction leads to different phase-transition temperatures or even different ground states [14]. Compared with the effective Hamiltonian method, our approaches allow us to investigate short-range interaction more precisely. Instead of taking the short-range interactions as a whole, we isolated anharmonic terms and studied how their energies changed with temperature. Although the bounding procedure provided 64 more energy terms to the model, their energies are close to zero. Therefore, in this paper, we only analyze the original 18 anharmonic terms of our model. Figures 9(a)–9(c) give the energy of different terms around R-O, O-T, and T-C phase-transition temperatures. The seventh and eighth energy terms are always dominant at different temperatures, and not all energy terms are essential to the phase transitions. The energy terms related to phase transitions are the 7th, 8th, 9th, 11th, and 12th. As is shown in Table I, these terms are all related to displacements of Ti and O atoms, which indicates the structural phase transition is driven by the interaction of Ti and O atoms.

Moreover, all the strain-coupling terms are third order, which is like that in the effective Hamiltonian method or Landau-Devonshire expansion [12], suggesting an explanation to why the effective Hamiltonian method can get the right phase-transition sequence without any high-order strain–phonon coupling included. Furthermore, we studied how these energy terms change with temperature. As is shown in Fig. 9(d), the phase transitions are accompanied by a sudden decrease or increase of different energy terms. A sudden decrease of the 9th, 11th, and 12th terms and increase of the 7th and 8th terms lead to the R-O phase transition. The competition between the 7th and 8th terms leads to the O-T phase transition, and the eighth term presents a T phase when it dominates. If we turned off the eighth term by modifying its parameter to zero, there only exists a directly phase transition from rhombohedral to cubic ∼190 K, as is shown in Fig. 10. In contrast with the case of the disappearance of the orthorhombic and tetragonal phases, when the homogeneous strain is fixed to zero, as reported in the Ref. [14], in this paper, we further reveal that the interaction between the strain and the Ti-O bond is responsible for the appearance of the correct phase-transition sequence.

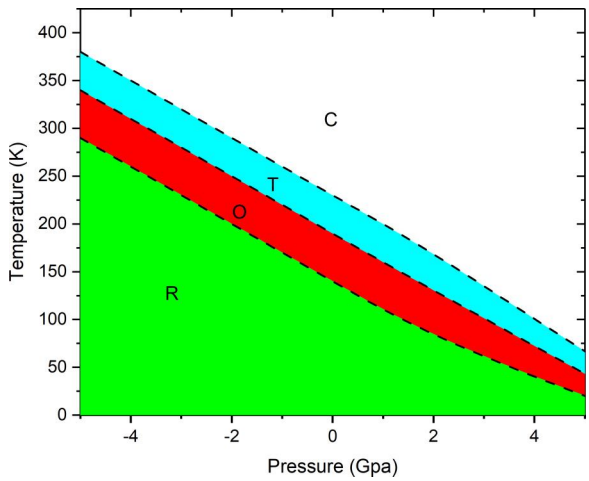

FIG. 8. Stress-temperature phase diagram of BTO from second-principles method.

D. Permittivity and *P-E* loops

Finally, we focus on the response of BTO to the external electric field. After the electric field is applied, there are two important features of ferroelectric materials, which are the peaks in dielectric permittivity around phase transitions and polarization–electric field hysteresis curves. The dielectric permittivity changes with temperature around the tetragonal-to-cubic phase transition are shown in Fig. 11(a). The electric field is applied in the z direction, and the dielectric permittivity is derived from the derivative of polarization to the electric field at zero field. The trend of the permittivity agrees well with experiment, in which the permittivity increases as the temperature goes up and the ferroelectric phase transition is

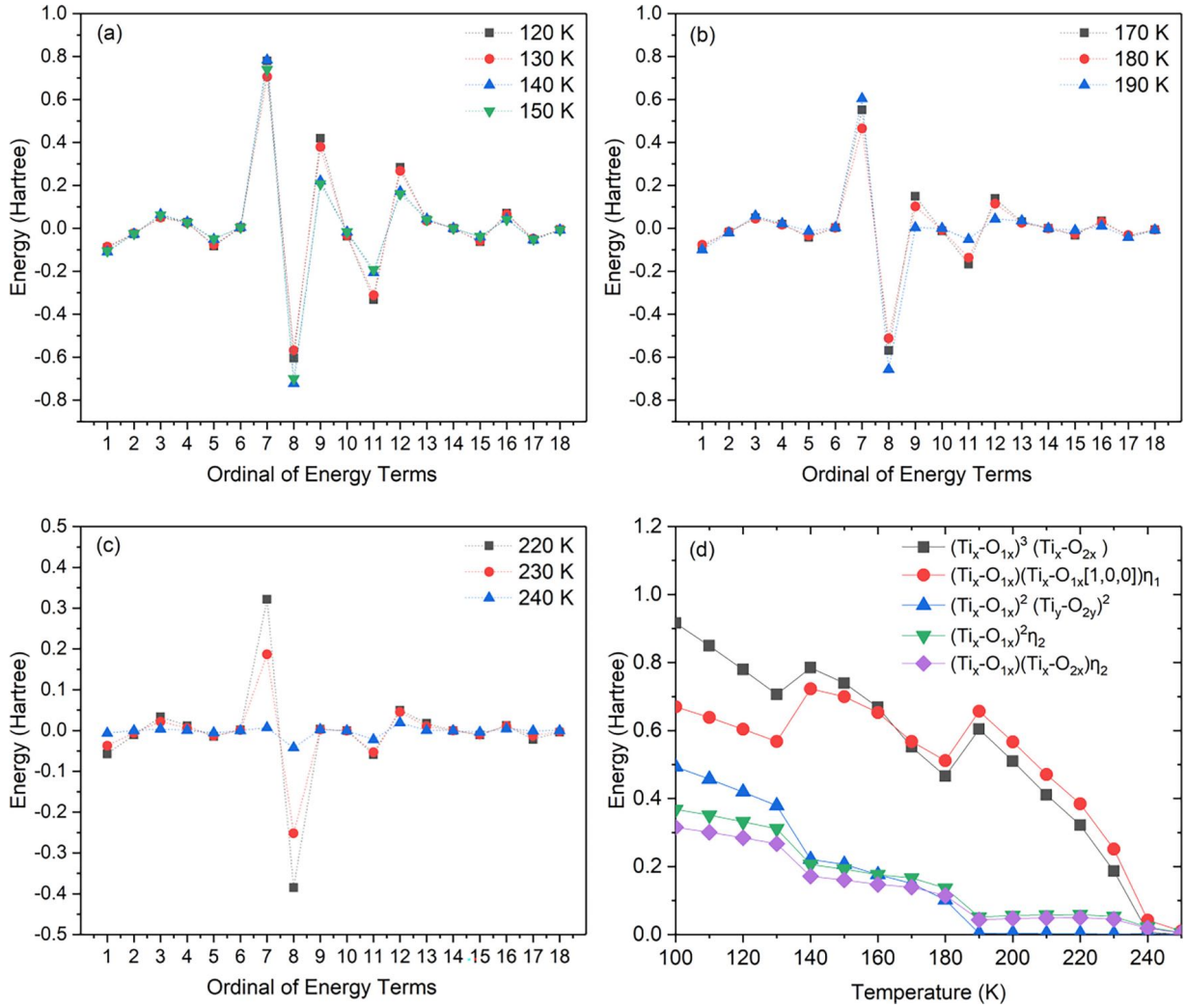

FIG. 9. (a)–(c) The energies of different terms in the potential energy of second-principles model. (d) Energies of different terms changes with temperature, in which there are abrupt changes for the seventh and eighth energy terms at the phase-transition temperatures of 130 and 180 K.

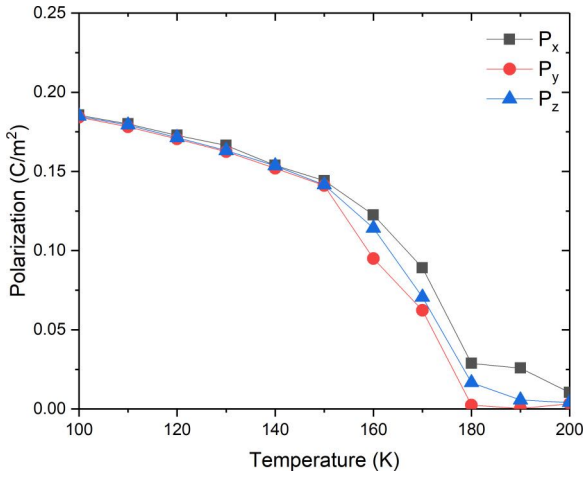

FIG. 10. Polarization changes with temperature once the eighth term of second-principles model is fixed to zero. The polarization in all three directions goes to zero at 180 K implying a direct phase transition from rhombohedral to cubic.

accompanied by peaks in the dielectric permittivity. The maximum value of ε_{33} is 7945.1, which is higher than experiment and the effective Hamiltonian results [41]. Figure 11(b) shows the inverse dielectric constant as a function of temperature, and it is fitted by $\varepsilon_{33}^{-1} = aT + b$. It can be seen clearly that there is a linear relationship between the inverse dielectric constant and temperature, and the ratio of the slope before and after phase transition is 7.2. These two properties indicate that there is an intrinsic first-order phase transition of BTO $\sim$ 224 K.

The polarization–electric field hysteresis curve (*P-E* loop) is another symbol for ferroelectric materials. In this paper, we simulated the *P-E* loop with the bounded second-principles model at zero temperature. The electric field is applied along the z-direction range from -0.0085 to $0.0085\,\mathrm{V/Å}$, and the polarization in the z direction changes with the electric field are shown in Fig. 12(a). From the hysteresis loop we have obtained, we can see that the coercive electric field is $0.00245\,\mathrm{V/Å}$, which agrees well with the experimental results measured at 77 K [45]. The domain structure before and after the coercive electric field are shown in Figs. 12(b) and 12(c).

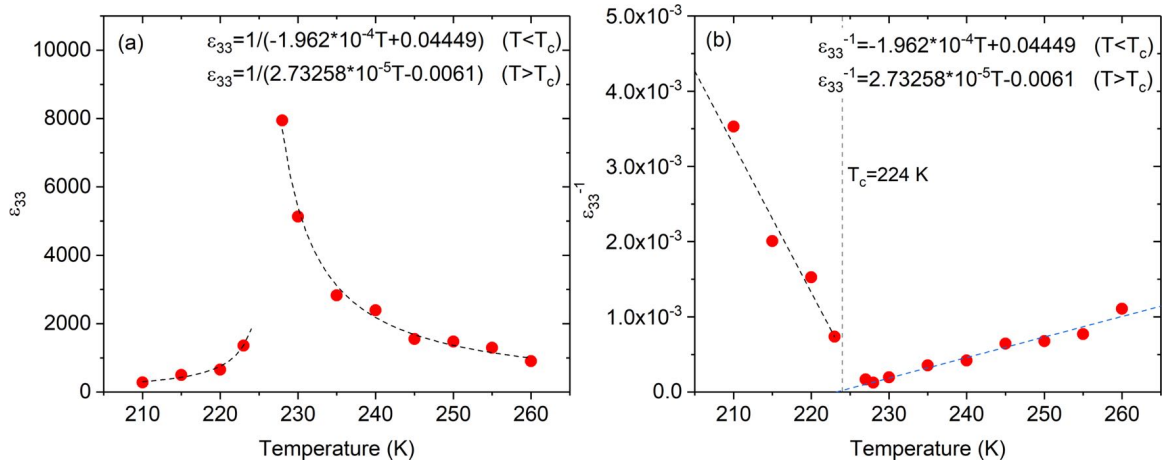

FIG. 11. Dielectric constant and inverse dielectric constant changes with temperature around the cubic to tetragonal phase transition.

IV. CONCLUSIONS

In summary, the atomistic second-principles model is built to describe the structure phase transition and dielectric properties of BTO. The model is validated by comparing energy and phonons of different phases, lattice constants, and polarization of the ground state with those of DFT calculation. Based on the second-principles model, the temperature-dependent lattice constants and polarization are obtained, and the R-O-T-C phase-transition sequence is captured, which is consistent with experimental results. With this model, the effects of external stress are also investigated. It is found that, in the absence of higher-order strain coupling terms, compared with experimental results, only the effect of stress on the O-T phase-transition temperature can be accurately captured. Furthermore, this method allows us to investigate short-range interaction more precisely than other methods. The calculation results show that the coupling between strain and the titanium-oxygen bond plays a decisive role in the phase-transition sequence. Finally, the dielectric permittivity and *P-E* loops are predicted by the model. The dielectric permittivity predicted by the model indicates an intrinsic first-order phase transition of BTO. In this paper, we provide insights into the phase transitions of BTO from the atomic level and expand the application of the second-principles method.

ACKNOWLEDGMENTS

This paper was supported by the National Program on Key Basic Research Project (Grant No. 2022YFB3807601), National Natural Science Foundation of China (Grants No. 12302208, No. 12272338, No. 12192214, and No. 11972320), and the Key Research Project of Zhejiang Laboratory (No. 2021PE0AC02). L.B., X.H., and P.G. acknowledges financial

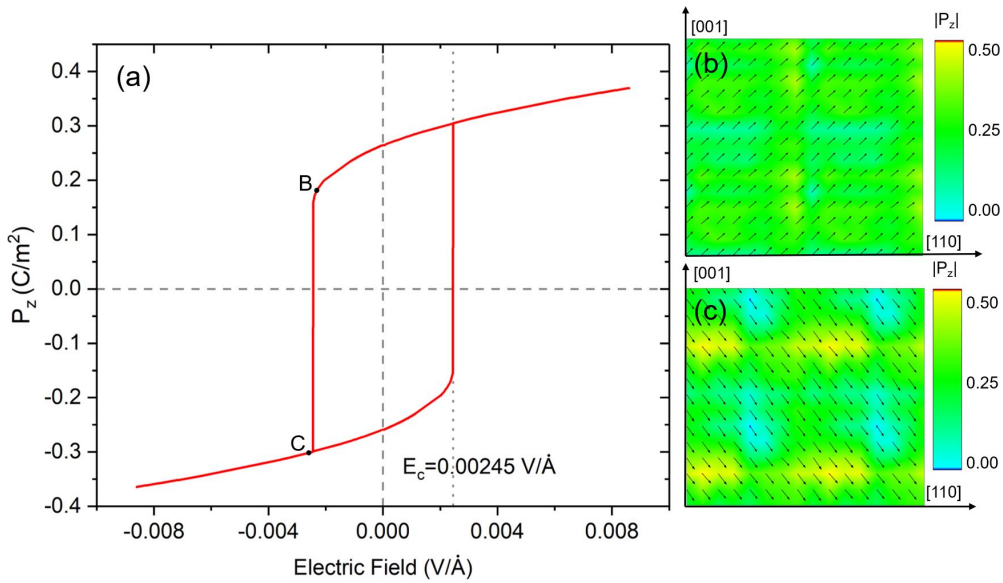

FIG. 12. (a) P_z-E loop of BTO at zero temperature. The electric field is applied on the z direction. The domain structure at point B and C are shown in (b) and (c).

support from F.R.S.-FNRS Belgium (grant PROMOSPAN) and the European Union's Horizon 2020 research and innovation program under Grant Agreement No. 964931 (TSAR). The authors also acknowledge access to the CECI supercomputer facilities funded by the F.R.S.-FNRS (Grant No. 2.5020.1) and to the Tier-1 supercomputer of the Fédération Wallonie-Bruxelles funded by the Walloon Region (Grant No. 1117545).

[1] M. Miura, B. Maiorov, T. Kato, T. Shimode, K. Wada, S. Adachi, and K. Tanabe, Strongly enhanced flux pinning in one-step deposition of $BaFe_2(As_{0.66}P_{0.33})_2$ superconductor films with uniformly dispersed $BaZrO_3$ nanoparticles, Nat. Commun. **4**, 2499 (2013).

[2] D. Pergolesi, E. Fabbri, A. D'Epifanio, E. Di Bartolomeo, A. Tebano, S. Sanna, S. Licoccia, G. Balestrino, and E. Traversa, High proton conduction in grain-boundary-free yttrium-doped barium zirconate films grown by pulsed laser deposition, Nat. Mater. **9**, 846 (2010).

[3] P. S. Dobal, A. Dixit, R. S. Katiyar, Z. Yu, R. Guo, and A. S. Bhalla, Micro-Raman scattering and dielectric investigations of phase transition behavior in the $BaTiO_3$–$BaZrO_3$ system, J. Appl. Phys. **89**, 8085 (2001).

[4] M. Acosta, N. Novak, V. Rojas, S. Patel, R. Vaish, J. Koruza, G. A. Rossetti Jr., and J. Rödel, $BaTiO_3$-based piezoelectrics: Fundamentals, current status, and perspectives, Appl. Phys. Rev. **4**, 041305 (2017).

[5] H. D. Megaw, Origin of ferroelectricity in barium titanate and other perovskite-type crystals, Acta Cryst. **5**, 739 (1952).

[6] Y. L. Li and L. Q. Chen, Temperature-strain phase diagram for $BaTiO_3$ thin films, Appl. Phys. Lett. **88**, 072905 (2006).

[7] R. E. Cohen and H. Krakauer, Lattice dynamics and origin of ferroelectricity in $BaTiO_3$: Linearized-augmented-plane-wave total-energy calculations, Phys. Rev. B **42**, 6416 (1990).

[8] R. A. Evarestov and A. V. Bandura, First-principles calculations on the four phases of $BaTiO_3$, J. Comput. Chem. **33**, 1123 (2012).

[9] R. Raffaele, *Ab initio* simulation of the properties of ferroelectric materials, Modelling Simul. Mater. Sci. Eng. **11**, R69 (2003).

[10] Y. Zhang, J. Hong, B. Liu, and D. Fang, Strain effect on ferroelectric behaviors of $BaTiO_3$ nanowires: A molecular dynamics study, Nanotechnology **21**, 015701 (2010).

[11] Z. Ma, L. Xi, H. Liu, F. Zheng, H. Gao, Z. Chen, and H. Chen, Ferroelectric phase transition of $BaTiO_3$ single crystal based on a tenth order Landau-Devonshire potential, Comput. Mater. Sci. **135**, 109 (2017).

[12] Y. L. Li, L. E. Cross, and L. Q. Chen, A phenomenological thermodynamic potential for $BaTiO_3$ single crystals, J. Appl. Phys. **98**, 064101 (2005).

[13] W. Zhong, D. Vanderbilt, and K. M. Rabe, Phase transitions in $BaTiO_3$ from first principles, Phys. Rev. Lett. **73**, 1861 (1994).

[14] W. Zhong, D. Vanderbilt, and K. M. Rabe, First-principles theory of ferroelectric phase transitions for perovskites: The case of $BaTiO_3$, Phys. Rev. B **52**, 6301 (1995).

[15] S. Tinte, M. G. Stachiotti, M. Sepliarsky, R. L. Migoni, and C. O. Rodriguez, Atomistic modelling of $BaTiO_3$ based on first-principles calculations, J. Phys. Condens. Matter **11**, 9679 (1999).

[16] J. M. Vielma and G. Schneider, Shell model of $BaTiO_3$ derived from *ab-initio* total energy calculations, J. Appl. Phys. **114**, 174108 (2013).

[17] Y. Qi, S. Liu, I. Grinberg, and A. M. Rappe, Atomistic description for temperature-driven phase transitions in $BaTiO_3$, Phys. Rev. B **94**, 134308 (2016).

[18] S. Tinte, J. Íñiguez, K. M. Rabe, and D. Vanderbilt, Quantitative analysis of the first-principles effective Hamiltonian approach to ferroelectric perovskites, Phys. Rev. B **67**, 064106 (2003).

[19] B. G. Dick and A. W. Overhauser, Theory of the dielectric constants of alkali halide crystals, Phys. Rev. **112**, 90 (1958).

[20] G. V. Gibbs, R. T. Downs, D. F. Cox, N. L. Ross, C. T. Prewitt, K. M. Rosso, T. Lippmann, and A. Kirfel, Bonded interactions and the crystal chemistry of minerals: A review, Z. Krist. Cryst. Mater. **223**, 01 (2008).

[21] R. He, H. Wu, L. Zhang, X. Wang, F. Fu, S. Liu, and Z. Zhong, Structural phase transitions in $SrTiO_3$ from deep potential molecular dynamics, Phys. Rev. B **105**, 064104 (2022).

[22] L. Gigli, M. Veit, M. Kotiuga, G. Pizzi, N. Marzari, and M. Ceriotti, Thermodynamics and dielectric response of $BaTiO_3$ by data-driven modeling, npj Comput. Mater. **8**, 209 (2022).

[23] N. Xu, Y. Shi, Y. He, and Q. Shao, A deep-learning potential for crystalline and amorphous Li–Si alloys, J. Phys. Chem. C **124**, 16278 (2020).

[24] L. Zhang, M. Chen, X. Wu, H. Wang, W. E., and R. Car, Deep neural network for the dielectric response of insulators, Phys. Rev. B **102**, 041121(R) (2020).

[25] J. C. Wojdeł, P. Hermet, M. P. Ljungberg, P. Ghosez, and J. Íñiguez, First-principles model potentials for lattice-dynamical studies: General methodology and example of application to ferroic perovskite oxides, J. Phys.: Condens. Matter **25**, 305401 (2013).

[26] P. Zubko, J. C. Wojdeł, M. Hadjimichael, S. Fernandez-Pena, A. Sené, I. Luk'yanchuk, J.-M. Triscone, and J. Íñiguez, Negative capacitance in multidomain ferroelectric superlattices, Nature (London) **534**, 524 (2016).

[27] M. A. Pereira Gonçalves, C. Escorihuela-Sayalero, P. Garca-Fernández, J. Junquera, and J. Íñiguez, Theoretical guidelines to create and tune electric skyrmion bubbles, Sci. Adv. **5**, eaau7023 (2019).

[28] H. Aramberri, N. S. Fedorova, and J. Íñiguez, Ferroelectric/paraelectric superlattices for energy storage, Sci. Adv. **8**, eabn4880 (2022).

[29] M. Torrent, F. Jollet, F. Bottin, G. Zérah, and X. Gonze, Implementation of the projector augmented-wave method in the ABINIT code: Application to the study of iron under pressure, Comput. Mater. Sci. **42**, 337 (2008).

[30] X. Gonze, A brief introduction to the ABINIT software package, Z. Krist. Cryst. Mater. **220**, 558 (2005).

[31] J. P. Perdew, A. Ruzsinszky, G. I. Csonka, O. A. Vydrov, G. E. Scuseria, L. A. Constantin, X. Zhou, and K. Burke, Restoring the density-gradient expansion for exchange in solids and surfaces, Phys. Rev. Lett. **100**, 136406 (2008).

[32] J. Laflamme Janssen, Y. Gillet, S. Poncé, A. Martin, M. Torrent, and X. Gonze, Precise effective masses from density functional perturbation theory, Phys. Rev. B **93**, 205147 (2016).

[33] X. Gonze, First-principles responses of solids to atomic displacements and homogeneous electric fields: Implementation of a conjugate-gradient algorithm, Phys. Rev. B **55**, 10337 (1997).

[34] X. Gonze and C. Lee, Dynamical matrices, Born effective charges, dielectric permittivity tensors, and interatomic force constants from density-functional perturbation theory, Phys. Rev. B **55**, 10355 (1997).

[35] C. Escorihuela-Sayalero, J. C. Wojdeł, and J. Íñiguez, Efficient systematic scheme to construct second-principles lattice dynamical models, Phys. Rev. B **95**, 094115 (2017).

[36] See Supplemental Material at http://link.aps.org/supplemental/10.1103/PhysRevB.108.134117 for all the anharmonic terms of bounded model; total energy and pressure change with time steps; phonon dispersion for rhombohedral phase of BTO from bounded model; and polarization and lattice constants changes with temperature from unbounded model.

[37] G. H. Kwei, A. C. Lawson, S. J. L. Billinge, and S. W. Cheong, Structures of the ferroelectric phases of barium titanate, J. Phys. Chem. C **97**, 2368 (1993).

[38] B. J. Campbell, H. T. Stokes, D. E. Tanner, and D. M. Hatch, ISODISPLACE: A web-based tool for exploring structural distortions, J. Appl. Crystallogr. **39**, 607 (2006).

[39] A. Togo, L. Chaput, T. Tadano, and I. Tanaka, Implementation strategies in PHONOPY and PHONO3PY, J. Phys. Condens. Matter **35**, 353001 (2023).

[40] A. Togo, First-principles phonon calculations with PHONOPY and PHONO3PY, J. Phys. Soc. Jpn. **92**, 012001 (2022).

[41] F. Mayer, M. N. Popov, D. M. Evans, S. Krohns, M. Deluca, and J. Spitaler, Improved description of the potential energy surface in $BaTiO_3$ by anharmonic phonon coupling, Phys. Rev. B **106**, 064108 (2022).

[42] A. Paul, J. Sun, J. P. Perdew, and U. V. Waghmare, Accuracy of first-principles interatomic interactions and predictions of ferroelectric phase transitions in perovskite oxides: Energy functional and effective Hamiltonian, Phys. Rev. B **95**, 054111 (2017).

[43] G. A. Samara, Pressure and temperature dependences of the dielectric properties of the perovskites $BaTiO_3$ and $SrTiO_3$, Phys. Rev. **151**, 378 (1966).

[44] R. E. Cohen, Origin of ferroelectricity in perovskite oxides, Nature (London) **358**, 136 (1992).

[45] O. Trithaveesak, J. Schubert, and C. Buchal, Ferroelectric properties of epitaxial $BaTiO_3$ thin films and heterostructures on different substrates, J. Appl. Phys. **98**, 114101 (2005).